



Targeted C-O bond cleavage of $^*\text{CH}_2\text{CHO}$ at copper active sites for efficient electrosynthesis of ethylene from CO_2 reduction

Huiying Zhang^a, Xiaojun Wang^a, Yanfei Sun^a, Xiaoxuan Wang^a, Zheng Tang^a, Shuyuan Li^a, Xueying Gao^a, Jinrui Wang^a, Zishan Hou^a, Kaiqi Nie^b, Jiangzhou Xie^{c,*}, Zhiyu Yang^{a,*}, Yi-Ming Yan^{a,*}

^a State Key Laboratory of Organic-Inorganic Composites, Beijing Advanced Innovation Center for Soft Matter Science and Engineering, Beijing University of Chemical Technology, Beijing 100029, People's Republic of China

^b Institute of High Energy Physics, Chinese Academy of Sciences, Beijing 100049, People's Republic of China

^c School of Mechanical and Manufacturing Engineering, University of New South Wales, Sydney, NSW 2052, Australia

ARTICLE INFO

Keywords:

CO_2 electroreduction
 $^*\text{CH}_2\text{CHO}$
 Selective bond breaking
 Cu-O bond
 Ethylene

ABSTRACT

$^*\text{CH}_2\text{CHO}$, a pivotal intermediate in CO_2 reduction reaction (CO_2RR) on copper-based catalysts, hinges on the strength of Cu-C and C-O bonds for the selective production of ethanol and ethylene. However, the targeted cleavage of these bonds at Cu active sites presents a formidable challenge. In this study, we manipulated the selective C-O bond breaking at Cu through an electron enrichment strategy, steering the reaction towards ethylene synthesis. Both experimental and theoretical investigations reveal that Gd incorporation elevates electron density at Cu sites, thereby enhancing Cu-O interaction and concurrently weakening the C-O bond at the critical Cu- $^*\text{O}-\text{CHCH}_2$ bifurcation point. Notably, Gd-doped Cu_2O (Gd- Cu_2O) demonstrated a 1.43-fold increase in the ethylene/ CO ratio relative to undoped Cu_2O . This alteration steers the reaction mechanism towards ethylene generation. Our study highlights the pivotal role of regulating reaction intermediates in optimizing activity and selectivity of CO_2RR in copper-based catalysts, providing valuable insights for future catalyst development.

1. Introduction

In the face of escalating atmospheric CO_2 levels, primarily driven by the overuse of fossil fuels, the electrocatalytic CO_2 reduction reaction (CO_2RR) emerges as a sustainable technological solution [1–7]. Utilizing renewable electricity, this method transforms CO_2 into valuable hydrocarbons and alcohols, offering a viable strategy for mitigating climate change and promoting a sustainable carbon cycle. The development of controllable electrocatalysts has consolidated the effectiveness of CO_2RR , capable of producing a variety range of products, including carbon monoxide (CO), methane (CH_4), ethylene (C_2H_4), and ethanol ($\text{C}_2\text{H}_5\text{OH}$) [8–15]. Among them, C_2 products, especially ethylene and ethanol, have significant industrial importance due to their wide application in the global chemical sector [16–21].

The mechanistic aspect of CO_2RR involves the pivotal role of intermediates adhering to the Cu active sites, forming a Cu-O-C bond [22–24]. This bond formation is critical in directing the subsequent

hydrogenation process towards either alkane or alcoholic organic compounds (Fig. 1a). The selectivity of the reaction hinges on the relative strengths of Cu-O and C-O bonds. The selective cleavage of Cu-O bonds produces mainly alcohols, while the cleavage of C-O bonds favors the production of alkanes [22,23]. This nuanced control over the bond cleavage processes enables the fine-tuning of product selectivity [25]. A case in point is the electrochemical catalytic synthesis of ethanol and ethylene, where the adsorption of the $^*\text{OCHCH}_2$ intermediate onto Cu active sites is crucial [23]. For examples, Edward H. Sargent et al. involved the development of a BaO/Cu catalyst with a unique interfacial structure [26]. This design was tailored to facilitate the breaking of Cu-O bonds, thereby regulating the selectivity of the reaction to produce higher alcohol yields. Moreover, Huang et al. engineered and synthesized cuprous cyanamide (Cu_2NCN) crystals [22]. This catalyst was specifically designed to disrupt the Cu-O bond interaction between the catalyst and the intermediate, promoting the formation of methanol. While advancements have been made in selectively breaking the Cu-O

* Corresponding authors.

E-mail addresses: jiangzhou.xie@unsw.edu.au (J. Xie), yangzhiyu@mail.buct.edu.cn (Z. Yang), yanyim22@mail.buct.edu.cn (Y.-M. Yan).

<https://doi.org/10.1016/j.apcatb.2024.123992>

Received 29 January 2024; Received in revised form 5 March 2024; Accepted 20 March 2024

Available online 21 March 2024

0926-3373/© 2024 Elsevier B.V. All rights reserved.

bond to increase ethanol yield, research in the selective cleavage of the C-O bond, specifically to enhance ethylene production, remains scant.

In this study, gadolinium (Gd), a rare earth metal with low electronegativity, was utilized as an electron donor to synthesize the Gd-Cu₂O electrocatalyst. This innovative catalyst modifies the electron density at Cu sites, facilitating selective cleavage of the C-O bond at the critical juncture of Cu-*O-CHCH₂. This adjustment in electron distribution effectively alters the CO₂ electroreduction pathway, favoring the production of C₂H₄. Comparative analysis showed a 1.42-fold increase in Faraday efficiency for the production of C₂H₄ over the Gd-Cu₂O (25.2%) catalyst compared to Cu₂O (17.8%), measured at -1.2 V versus the reversible hydrogen electrode (RHE), which serves as the reference point for all potentials in this research. The experimental results demonstrated that the Gd-Cu₂O catalyst maintains consistent C₂H₄ output over seven hours of continuous operation. This sustained performance is ascribed to the electron transfer from Gd to Cu, resulting in an elevated electron concentration at the Cu sites within the Gd-Cu₂O structure. Advanced theoretical calculations, including density of states (DOS), crystal orbital Hamilton population (COHP), and Bader analysis, confirmed these findings. They collectively show that the increase in electron density on Cu not only strengthens the Cu-O bond, but also accelerates the breaking of the C-O bond, thus improving ethylene selectivity. In situ Raman spectroscopy and Fourier transform infrared spectroscopy (FTIR) further support these conclusions. These techniques have elucidated that Gd-Cu₂O catalyst not only significantly inhibit hydrogen evolution, but also promote the formation of *CO and *OC-CO coupling mechanism. The findings of the research provide a new pathway for the actual conversion of CO₂ to C₂H₄, demonstrate the ability to selectively break and form bonds, and provide pathways for electrosynthesis of high-value products.

2. Experimental section

2.1. Synthesis of electrocatalysts

Cu₂O was prepared according to previously published literature. First, 0.909 g of copper(II) acetate was solubilized in 90 mL of fresh deionized water. Then, 100 mL of 0.35 M sodium hydroxide solution

was dripped into the above solution and stirred for 30 min. Next, drop 50 mL of 0.1 M ascorbic acid added to the solution, heated to 55 °C and mixed at this temperature for 50 minutes. The samples were centrifuged, washed several times with ethanol and water, and dried overnight in a vacuum oven at 70 °C. The Gd-Cu₂O catalyst was prepared by adopting the similar procedure for the Cu₂O synthesis as described above, Add 189 mg of Gd (NO₃)₃·6 H₂O to the back-facing mixture of the last part.

2.2. Characterizations

The X-ray diffraction (XRD, Rigaku D/max 2500) patterns were recorded with Cu K α radiation ($\lambda=0.15405$ nm) to analyze crystalline structures. Field emission scanning electron microscopy (SEM, FEI Quanta 200), Transmission electron microscopy (TEM, FEI Tecnai G220), high-resolution TEM (HRTEM, JEM-2100 F, 200 kV) corresponding energy dispersive X-ray (EDX) elemental mapping was performed to characterize the morphology and structure of the samples. Surface chemical states and compositions were obtained by X-ray photoelectron spectroscopy (XPS, Thermo Fisher Scientific) using Al K α X-rays as the excitation source. The soft XAS measurements were performed in total electron yield mode under ultra-high vacuum at beamline 4B9B. Ultraviolet photoelectron spectroscopy (UPS) measurements were performed on Thermo Scientific ESCALab 250Xi. In situ Raman spectra was collected in the range of 200–2200 cm⁻¹ on a 532 nm Finder Vista Laser micro-Raman Spectroscopy (Zolix, China). The applied bias was -1.0 to -1.4 V vs. RHE, and other parameters were the same as those used for CO₂RR performance tests.

2.3. Electrochemical measurements

The electrochemical measurements were conducted in a three-electrode system, making use of the CHI 660e electrochemical workstation. The anode and cathode electrolyte areas were separated by a cation-exchange membrane (Nafion 117 DuPont). Toray carbon paper with an active area of 1 cm² was used as working electrode. The counter and reference electrode were the Pt-plate and the Ag/AgCl (in saturated KCl solution) electrode, respectively.

All potentials were measured against an Ag/AgCl reference electrode

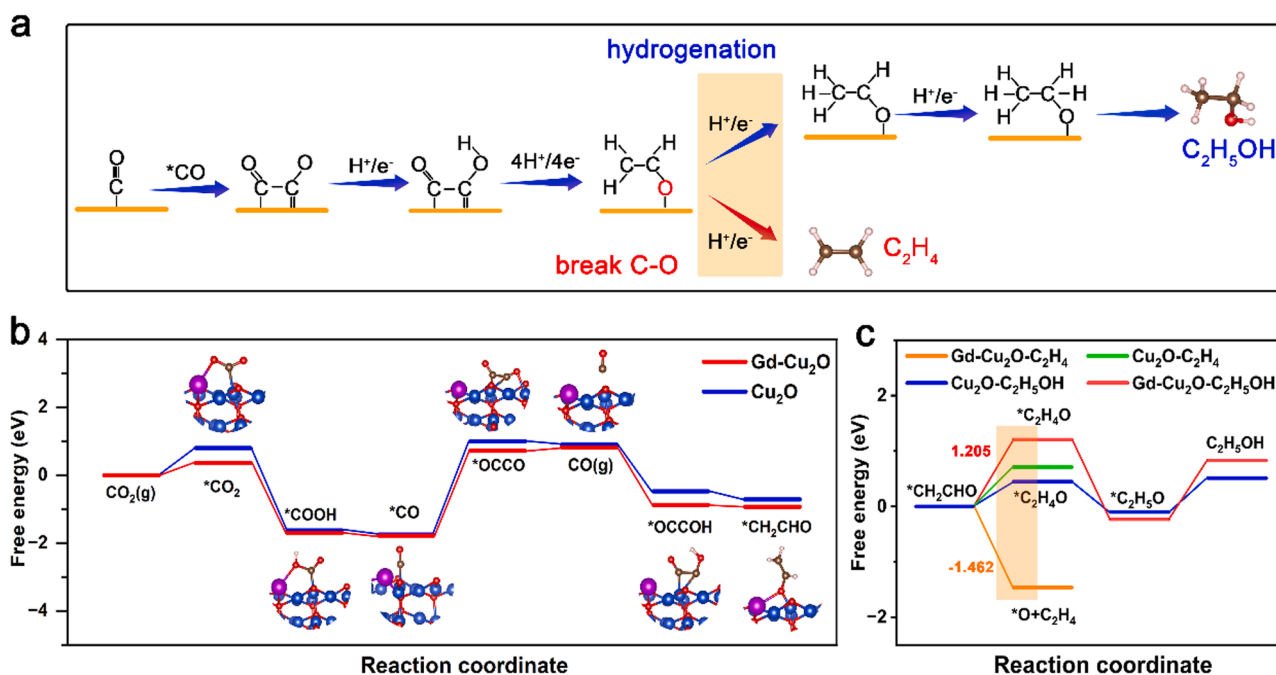


Fig. 1. (a) Schematic diagram of ethylene and ethanol generation pathways in CO₂RR. (b) Free-energy diagram for the CO₂RR on Gd-Cu₂O (111) and Cu₂O (111). (c) Free-energy diagrams of the C₂H₄ pathway and C₂H₅OH on Gd-Cu₂O (111) and Cu₂O (111).

and converted to the RHE reference scale following the equation:

$$E \text{ (vs RHE)} = E \text{ (vs Ag/AgCl)} + 0.0197 + (0.0591 \times \text{pH})$$

The 0.5 M KHCO₃ electrolyte is flushed with an Ar- or CO₂- stream for at least 30 minutes prior to the measurement. Gaseous and liquid products were obtained by conducting controlled-potential electrolysis at each potential for 60 min, and were collected and detected by gas chromatography (TECHCOMP GC7900II) and nuclear magnetic resonance (NMR, Bruker AVANCE AV III 400), respectively.

2.4. Computational details

We have performed density-functional theory (DFT) calculations using the Perdew-Burke-Ernzerhof (PBE) formula, employing first principles. All our calculations consider DFT-DF3 corrections. A critical value of the kinetic energy set at 450 eV and a k-point grid with a spacing of about 0.04 Å⁻¹ is used. Vacuum space is 20 Å along the z-axis. The Gibbs free energy change was calculated as follows:

$$G = E + \text{ZPE} - TS$$

3. Results and discussion

3.1. Calculation of adsorption energy of intermediates

Density functional theory (DFT) calculations were employed to illustrate the energetics of CO₂RR on Cu₂O and Gd-Cu₂O surfaces. Structural models for Gd-Cu₂O (111) and Cu₂O (111) were developed, denoted as Gd-Cu₂O and Cu₂O respectively (Fig. S1). The optimized configurations of these adsorption intermediates are depicted in Fig. 1b for Gd-Cu₂O and in Fig. S2 for Cu₂O. Notably, Gd-Cu₂O demonstrates a marked preference for *CO₂ formation, with the free energy of adsorption of 0.36 eV, significantly lower (by 0.44 eV) than that on Cu₂O. This suggests an enhanced capability of Gd-Cu₂O for CO₂ activation. Further, the formation of *OCCO on Gd-Cu₂O (0.72 eV) is thermodynamically more favorable compared to Cu₂O (1.00 eV), indicating a higher propensity of Gd-Cu₂O for generating C₂+ products. Additionally, the free energy profiles for hydrogen evolution reaction (HER) catalyzed by Gd-Cu₂O and Cu₂O were calculated and presented in Fig. S3. The results reveal a higher selectivity of Gd-Cu₂O for CO₂RR, attributed to its greater adsorption energy for *H. The energetics of ethylene and ethanol production, sharing the *OCHCH₂ intermediate, are detailed in Fig. S4 and S5. It was observed that the adsorbed *OCHCH₂ can progress to ethanol through several protonation steps, whereas ethylene is produced by protonation of C₂H₃ following the cleavage of the C-O bond in *OCHCH₂. On Gd-Cu₂O, the energy barrier for ethanol formation from *OCHCH₂ is endergonic (1.205 eV) (Fig. 1c), while ethylene production remains exergonic (-1.462 eV). Contrarily, on Cu₂O, the scenario is reversed, indicating a preference of Gd-Cu₂O for ethylene over ethanol production. To probe the electron density changes on Cu atoms following Gd introduction, differential charge density analyses were conducted. These analyses reveal yellow and blue regions, signifying electron accumulation and depletion, respectively (Fig. S6). The Gd-Cu₂O sample, in contrast to pure Cu₂O, shows significant charge rearrangement surrounding the Gd-doping area, with a pronounced transfer of charge from Gd to Cu atoms, denoting electron enrichment at the Cu sites. From the analysis presented, it is evident that Gd-Cu₂O possesses a reduced energy barrier for ethanol generation, attributable to the electron enrichment at Cu sites. This enrichment plays a key role in promoting the cleavage of the C-O bond in the *OCHCH₂ intermediate, thereby promoting the subsequent formation of C₂H₄.

3.2. Characterizations of Gd-Cu₂O Materials

Guided by theoretical calculations, we synthesized a Gd-Cu₂O catalyst using the wet chemical reduction method [27], as depicted in Fig. 2a. The composition of the synthesized Gd-Cu₂O catalyst, specifically the Gd content, was quantified using inductively coupled plasma optical emission spectrometry (ICP-OES) (Table S1). The results revealed a Gd doping level of 3.832 wt% in the Gd-Cu₂O, confirming the successful incorporation of Gd atoms in place of some Cu atoms [28,29]. We investigated the crystal structures of the synthesized materials using X-ray diffraction (XRD) analysis. As illustrated in Fig. 2b, the diffraction patterns of Gd-Cu₂O closely match those of pure Cu₂O (JCPDS 74-1230), with no distinct Gd phases detected [30]. This suggests that the Gd content in Gd-Cu₂O is minimal and below the detection threshold. Notably, the (111), (200), and (220) facet peaks of Gd-Cu₂O exhibit a slight shift to lower diffraction angles of approximately 0.06° compared to pure Cu₂O (Fig. 2c). This shift is attributed to the introduction of Gd, which has a larger atomic radius than Cu [31–34]. The Raman spectrum of pure Cu₂O, featuring a prominent peak at 213 cm⁻¹, is characteristic of Cu⁺ species (Fig. 2d). In contrast, the Raman peak of Gd-Cu₂O displays a subtle positive shift, indicating an interaction between Gd and Cu₂O [35]. Further insights into the Cu valence in the catalyst were obtained from the Cu LMM Auger spectrum (Fig. S7). The presence of a single peak at 916.6 eV confirmed that only Cu⁺ species were present in the Gd-Cu₂O [36–39]. The morphological characteristics of Gd-Cu₂O and pure Cu₂O were examined using scanning electron microscopy (SEM) (Fig. 2e and S8) and transmission electron microscopy (TEM) (Fig. 2 f and S8). The high-resolution TEM (HRTEM) image of Gd-Cu₂O revealed a lattice spacing of 0.251 nm [40–43], corresponding to the Cu₂O (111) plane (Fig. 2 g), and showcased structural features consistent with pure Cu₂O (Fig. S9). Energy-dispersive X-ray spectroscopy (EDX) elemental mapping of the samples (Fig. 2 h and S10) showed a uniform distribution of Cu, O, and Gd in Gd-Cu₂O. This comprehensive characterization confirms the successful integration of Gd into the Cu₂O lattice.

3.3. Characterizations of electronic structure

To investigate the impact of Gd incorporation on the electron density surrounding Cu atoms in Cu₂O, we conducted a series of analyses including X-ray photoelectron spectroscopy (XPS), soft X-ray absorption spectra, ultraviolet photoelectron spectroscopy (UPS), and theoretical calculations. Fig. 3a presents the Cu 2p XPS spectra of pure Cu₂O, which could be deconvoluted into four dominant peaks. These peaks correspond to Cu²⁺ (2p_{1/2} at 954.00 eV and 2p_{3/2} at 934.10 eV) and Cu⁺ (2p_{1/2} at 951.80 eV and 2p_{3/2} at 932.25 eV) [44–47]. Additionally, the Gd 4d XPS spectra (Fig. 3b) for Gd₂O₃ standard samples were analyzed and revealed two major peaks at 143.28 eV (4d_{5/2}) and 148.58 eV (4d_{3/2}) [48]. The peak at 143.28 eV is indicative of Gd³⁺, while the peak at 148.58 eV is associated with metallic Gd. Upon comparison, the Cu 2p spectra of Gd-Cu₂O exhibited a noticeable shift towards lower binding energy relative to pure Cu₂O. Concurrently, the Gd 4d spectra of Gd-Cu₂O shifted towards higher binding energy compared to the Gd₂O₃ standard. These binding energy shifts in the Gd-Cu₂O sample suggest that the introduction of Gd atoms leads to electron transfer from Gd to Cu sites [49,50]. Further substantiation of this electron enrichment is provided by the altered Cu 2p spectra in Gd-Cu₂O, which demonstrate a significant increase in the Cu⁺ / (Cu⁺ + Cu²⁺) peak area ratio to 69%, compared to 61% in pure Cu₂O. This higher ratio in Gd-Cu₂O strongly supports the notion of electron enrichment in the Cu component. Further substantiating the electron density variations in Gd-Cu₂O, we employed soft X-ray absorption spectroscopy (sXAS) [51] (Fig. 3c and 3d). The Cu L-edge and O K-edge sXAS spectra of Gd-Cu₂O exhibit a discernible shift towards the lower energy region in comparison with pure Cu₂O. These shifts in the sXAS peaks are indicative of an electron enrichment at Cu and O atoms in the Gd-Cu₂O samples, suggesting alterations in their

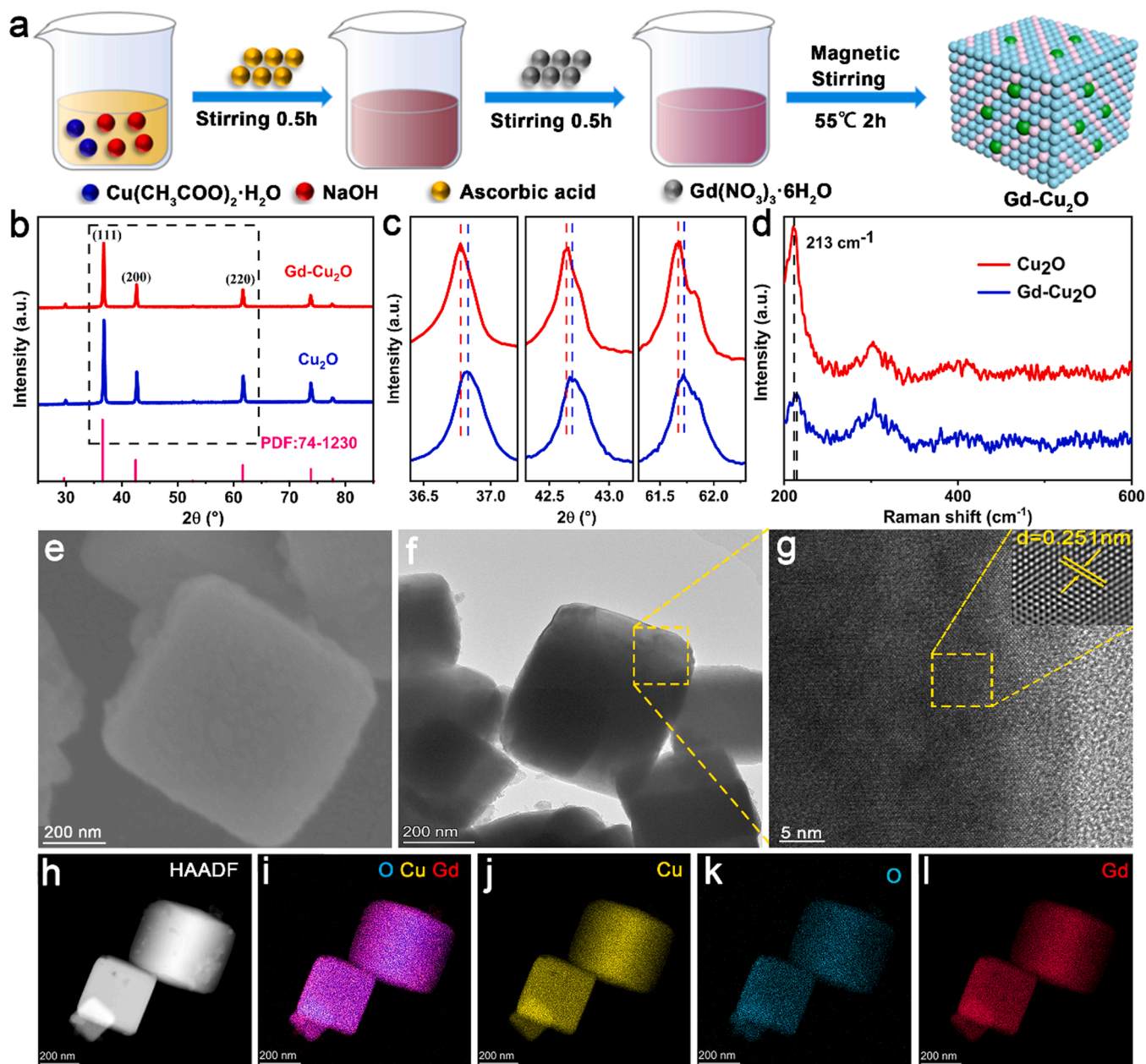


Fig. 2. (a) Schematic illustration of Gd-Cu₂O synthesis. (b) XRD patterns for Gd-Cu₂O and Cu₂O. (c) Enlarged view of the XRD patterns in the regions of the diffraction peaks of (111), (200), and (220) facet. (d) Raman spectra of Gd-Cu₂O and Cu₂O. (e) SEM and (f) TEM images of Gd-Cu₂O. (g) HRTEM image of the selected region in (f). (h) Elemental mapping images of Gd-Cu₂O.

electronic structure. To delve deeper into the electronic density of these materials, we utilized ultraviolet photoelectron spectroscopy (UPS) [52, 53]. The UPS spectra, recorded under an applied bias voltage, revealed cutoff energies (E_{cutoff}) of 17.65 eV for Gd-Cu₂O and 17.01 eV for Cu₂O (Fig. 3e). Correspondingly, the Fermi energy (E_f) values were determined to be 1.45 eV for Gd-Cu₂O and 1.03 eV for Cu₂O (Fig. 3f). Based on the equation $\Phi = h\nu - |E_{\text{cutoff}} - E_f|$ [54], the relevant work functions (Φ) of Gd-Cu₂O and Cu₂O were calculated to be 5.02 eV and 5.24 eV, respectively. This result implies a greater electron mobility within Gd-Cu₂O compared to Cu₂O, enhancing the interaction between the catalyst and reaction intermediates.

To elucidate the effect of electron enrichment at active sites on the adsorption of intermediates, we conducted DFT calculations. The PDOS analysis of O 2p orbitals on Cu₂O surfaces, a crucial descriptor for assessing the Cu-O bond strength, revealed a noticeable peak shift towards the antibonding direction (Fig. 3g). This shift indicates relatively

stronger Cu-O bond in Gd-Cu₂O compared to Cu₂O [22]. Further, the PDOS of both Gd-Cu₂O and Cu₂O was examined (Fig. 3h). Notably, the d-band center of pure Cu₂O is located further from the Fermi level compared to that of Gd-Cu₂O. This observation leads to a preliminary conclusion that Gd-Cu₂O exhibits stronger surface activation towards intermediates, such as *OCHCH₂, than Cu₂O [55]. This is manifested in the increased C-O bond length on the Gd-Cu₂O surface (Fig. 3i). The elongation of the C-O bond suggests a facilitated bond cleavage, implying a preference for C₂H₄ formation in the catalytic process. The analysis underscores that the introduction of Gd into Cu₂O leads to electron enrichment at the Cu atoms, thereby enhancing the interaction with the intermediate *OCHCH₂. This enhanced interaction strengthens the Cu-O bond and promotes the breaking of the C-O bond, steering the reaction pathway towards the formation of C₂H₄.

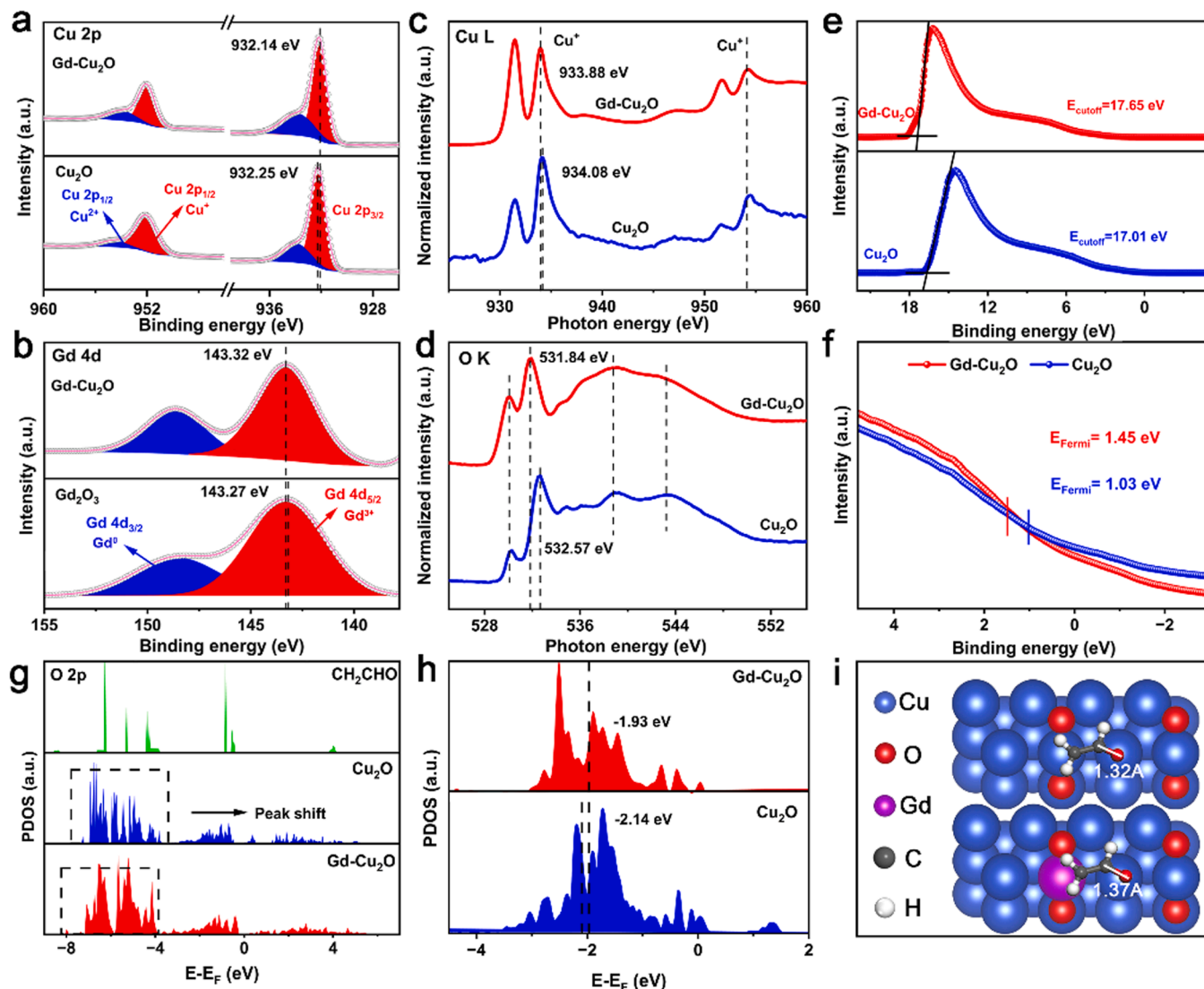


Fig. 3. XPS profiles of (a) Cu 2p and (b) Gd 4d for Gd-Cu₂O, Cu₂O and (standard) Gd₂O₃. (c) sXAS Cu L-edge spectra of Gd-Cu₂O and Cu₂O. (d) sXAS O K-edge spectra of Gd-Cu₂O and Cu₂O. (e) Secondary electron cutoff edge and (f) Fermi edge of Gd-Cu₂O and Cu₂O acquired by UPS. (g) PDOS curves of the O 2p orbitals of free *OCHCH₂ and of *OCHCH₂ adsorbed on Cu₂O (111) and Gd-Cu₂O (111). (h) PDOS of d-band for Cu₂O (111) and Gd-Cu₂O (111) catalysts. (i) Schematic illustration of key intermediate *OCHCH₂ to yield C₂H₄ and EtOH over Cu₂O (111) and Gd-Cu₂O (111) surfaces.

3.4. Electrocatalytic activity for CRR

The electrocatalytic performance of the synthesized products was preliminarily evaluated using a standard H-cell in CO₂-saturated 0.5 M KHCO₃ solution. Linear sweep voltammetry (LSV) tests, conducted with a three-electrode system in both CO₂-saturated and Ar-saturated 0.5 M KHCO₃ electrolytes, provided insights into their catalytic activities. As illustrated in Fig. 4a, the LSV curves highlight that both Gd-Cu₂O and Cu₂O catalysts exhibit augmented current densities under a CO₂ atmosphere compared to those under an Ar atmosphere, underscoring their enhanced catalytic efficiencies for CO₂RR. Significantly, the Gd-Cu₂O catalyst demonstrates markedly higher activity, achieving a current density of 34.66 mA cm⁻² at -1.2 V, surpassing the performance of pure Cu₂O in the CO₂-saturated electrolyte. The composition of the gas and liquid products was determined using gas chromatography (GC) and ¹H nuclear magnetic resonance (NMR) spectroscopy (Fig. 4b-d). The Faraday efficiencies (FEs) of the primary products, CO and C₂H₄, for both catalysts were analyzed over a potential range of -1.0 V to -1.4 V, with additional reduction products detailed in Fig. S11 and S12. This comparative analysis reveals that the FEs of Gd-Cu₂O for ethylene

production are substantially higher than those of the pure Cu₂O sample across the entire potential range. Notably, at -1.2 V, the peak FE for C₂H₄ production is 25.2% for Gd-Cu₂O and 17.8% for pure Cu₂O. These findings suggest that the electron enrichment effect at the Cu sites in Gd-Cu₂O enhances the Cu-O interaction, facilitates the breaking of the C-O bond, and preferentially steers the reaction towards the formation of ethylene, while concurrently suppressing ethanol production. To mitigate potential variability in FE, we have implemented error bars in our analysis. The data presented in Fig. S13-14 reveal minimal differences between parallel experiments, thereby reinforcing the reproducibility of our findings. Furthermore, all parallel experiment data have been displayed in Fig. S15-16. Furthermore, as illustrated in Fig. 4e-f, there is a notable surge in the production of ethylene and carbon monoxide during the initial phase of the experiment. This increase can primarily be attributed to the generation of abundant Cu⁺ and Cu⁰ sites, alongside significant bulk reconstruction, which collectively facilitate the generation of C₂H₄ and CO [56]. It is important to note, however, that excessive reconstruction and the intensification of the HER can adversely impact the selectivity for these products. Consequently, the FE for ethylene and carbon monoxide may decrease over time.

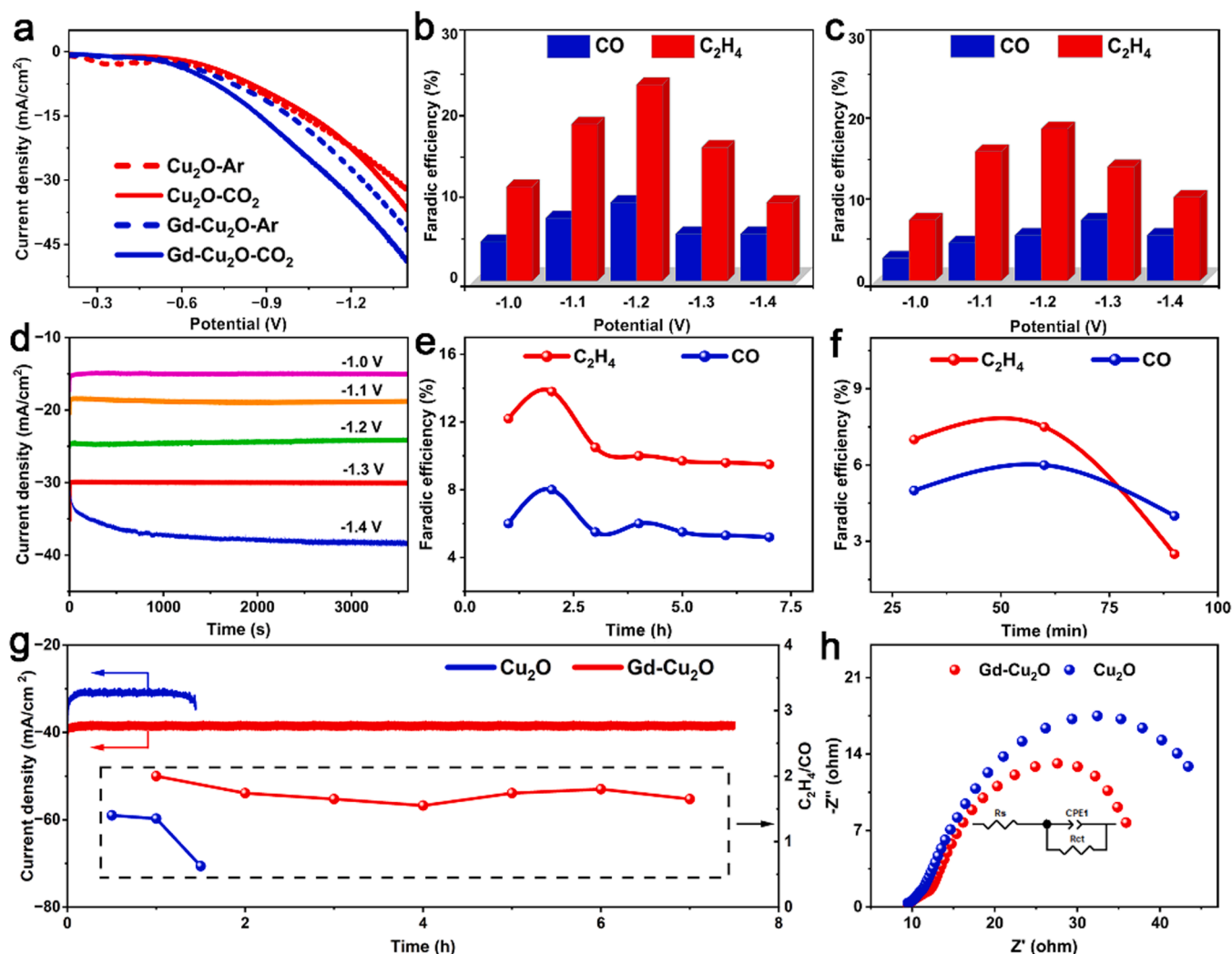


Fig. 4. (a) Linear sweep voltammetry curves of Gd-Cu₂O and Cu₂O in Ar-saturated and CO₂-saturated 0.5 M KHCO₃ aqueous. The Faradic efficiencies of CO and C₂H₄ for (b) Gd-Cu₂O and (c) Cu₂O electrolyzed in 0.5 M KHCO₃ electrolyte for 1 h. (d) Electrolysis curves at different applied potentials for Gd-Cu₂O. CO and C₂H₄ Faradic efficiencies for Gd-Cu₂O (e) and Cu₂O (f) functioning of electrolysis time at -1.2 V. (g) The i-t curves and C₂H₄/CO ratios of Gd-Cu₂O and Cu₂O at a fixed potential of -1.2 V. (h) Nyquist charts of Gd-Cu₂O and Cu₂O in 0.5 M KHCO₃.

The electrochemical stability of the catalysts was further investigated at -1.2 V.

Fig. 4e illustrates the performance of the Gd-Cu₂O catalyst during a 7-hour electrolysis test. Remarkably, only a slight decay of C₂H₄ (approximately 31.15%) and CO (approximately 31.25%) in FE was observed. In sharp contrast, C₂H₄ (approximately 67.7%) and CO (approximately 24.5%) rapidly decays pure Cu₂O within 1.5 hours (Fig. 4f). The precipitous decline in FE for C₂H₄ and CO in the case of pure Cu₂O, potentially caused by its reconstitution, suggests its swift degradation under similar conditions. Given that C₂H₄ and CO are the primary products for both Gd-Cu₂O and pure Cu₂O, we used the C₂H₄/CO ratio as an indicator of the catalysts' stability. As depicted in Fig. 4g, the Gd-Cu₂O catalyst maintained a relatively stable C₂H₄/CO ratio (ranging from 2.00 to 1.65) throughout the 7-hour test, indicating consistent selectivity. Conversely, the ratio for Cu₂O plummeted from 1.40 to 0.63 within 1.5 hours, underscoring its significantly poorer stability and selectivity for C₂ products. To further confirm the stability of Cu⁺ species, we conducted in situ Raman measurements at a potential of -1.2 V. Both Gd-Cu₂O and pure Cu₂O exhibited Raman signals at 213 cm⁻¹ (Fig. S17), characteristic of Cu⁺ species [56,57]. Intriguingly, under operando conditions, the Raman peak for Gd-Cu₂O remained observable for over 20 minutes (Fig. S17a). However, for pure Cu₂O, the

Raman signals vanished within 12 minutes (Fig. S17b), indicative of the reduction of Cu₂O to metallic Cu. It should be noted that the red signal in Fig. S17 predominantly stems from a baseline shift, altering background intensity. We further investigated the structural transformation of Gd-Cu₂O and Cu₂O under electrochemical conditions at -1.2 V using ex-situ XRD (Fig. S18). For the Gd-Cu₂O samples (Fig. S18a), a notable change was observed during 1 hour of electrolysis: the intensity of the characteristic Cu₂O (111) and Cu₂O (200) peaks gradually diminished, while the intensity of the Cu (111) peak increased, suggesting a structural transformation. In stark contrast, the pure Cu₂O sample (Fig. S18b) underwent a rapid reduction to metallic Cu within just 30 minutes. This was evidenced by the disappearance of the Cu₂O (111) peak and a significant increase in the intensity of the Cu (111) peak, underscoring the enhanced stability of Cu⁺ species in the Gd-Cu₂O [58]. To further probe the kinetics of these electrocatalytic reactions, we performed electrochemical impedance spectroscopy (EIS) measurements [59]. The results reveal that Gd-Cu₂O exhibits a lower interfacial charge transfer resistance compared to pure Cu₂O (Fig. 4h). This observation indicates that Gd-Cu₂O facilitates more rapid electron transfer during CO₂RR process, which is a critical factor in enhancing the efficiency and efficacy of the catalytic activity. This suite of structural and electrochemical analyses collectively demonstrates the superiority of Gd-Cu₂O over Cu₂O in terms

of both stability and charge transfer kinetics, providing valuable insights into the mechanistic aspects of their electrocatalytic performance.

3.5. In situ measurements and DFT calculation

To probe reaction intermediates and elucidate the mechanism underlying CO₂RR catalytic process, in situ Fourier Transform Infrared (FTIR) and in situ Raman spectroscopy analyses were performed under potentials ranging from -1.0 V to -1.4 V, as well as at open-circuit potential (OCP) in a 0.5 M KHCO₃ electrolyte. The in situ FTIR spectra revealed distinct differences between the pure Cu₂O and Gd-Cu₂O catalysts. For pure Cu₂O, the FTIR spectrum was dominated by signals related to the hydrogen evolution reaction (HER) during CO₂RR (Fig. 5a). This is evidenced by the presence of stretching vibrations of CO₃²⁻ (ν CO₃²⁻) and H₂O (δ H₂O) at around 1401 and 1657 cm⁻¹ [60,61], respectively, and only a faint *CO peak appearing at -1.4 V. In stark contrast, the Gd-Cu₂O (Fig. 5b) exhibited a prominent CO adsorption vibration signal near 2040 cm⁻¹ [62,63], emerging at a potential of -1.1 V. This signal, which intensifies with increasing overpotentials, indicates a higher adsorption capacity for *CO on the Gd-Cu₂O surface. The enhanced *CO coverage is favorable for subsequent C-C coupling

reactions, leading to the formation of C₂ products. Complementing the FTIR findings, in situ Raman spectroscopy (Fig. S19) provided further compelling evidence of the superior capability of Gd-Cu₂O to generate more *CO, enhance *CO coverage on the catalyst surface, and promote the formation of C₂ products. This suite of spectroscopic data not only highlights the distinct catalytic behaviors of Gd-Cu₂O and Cu₂O but also underscores the enhanced efficiency of Gd-Cu₂O in facilitating CO₂RR, particularly in the formation of value-added C₂ products.

To elucidate the CO₂RR mechanism, DFT calculations were performed, comparing the CO₂RR selectivity on Gd-Cu₂O with that on Cu₂O (111). Our analysis focused on the hydrogenation pathways and the disruption of the C-O bond, leaving a residual *O. Hydrogenation leading to *OCHCH₃ formation was identified as conducive to ethanol generation, while the breaking of the *O-CHCH₂ bond facilitates ethylene formation. We propose the relative bond strength of Cu- and *O-CHCH₂ as a descriptor for ethylene selectivity and utilized crystal orbital Hamilton population (COHP)[64] and Bader charge density analysis[26] to quantify charge transfer in Cu-COH and C-OH, proxies for bond strength. As shown in Fig. 5c and 5d, the bonding orbital of Cu-O in Gd-Cu₂O (-ICOHP: 4.519) exhibits greater occupancy than that in Cu₂O (-ICOHP: 2.931), suggesting a stronger Cu-O interaction in

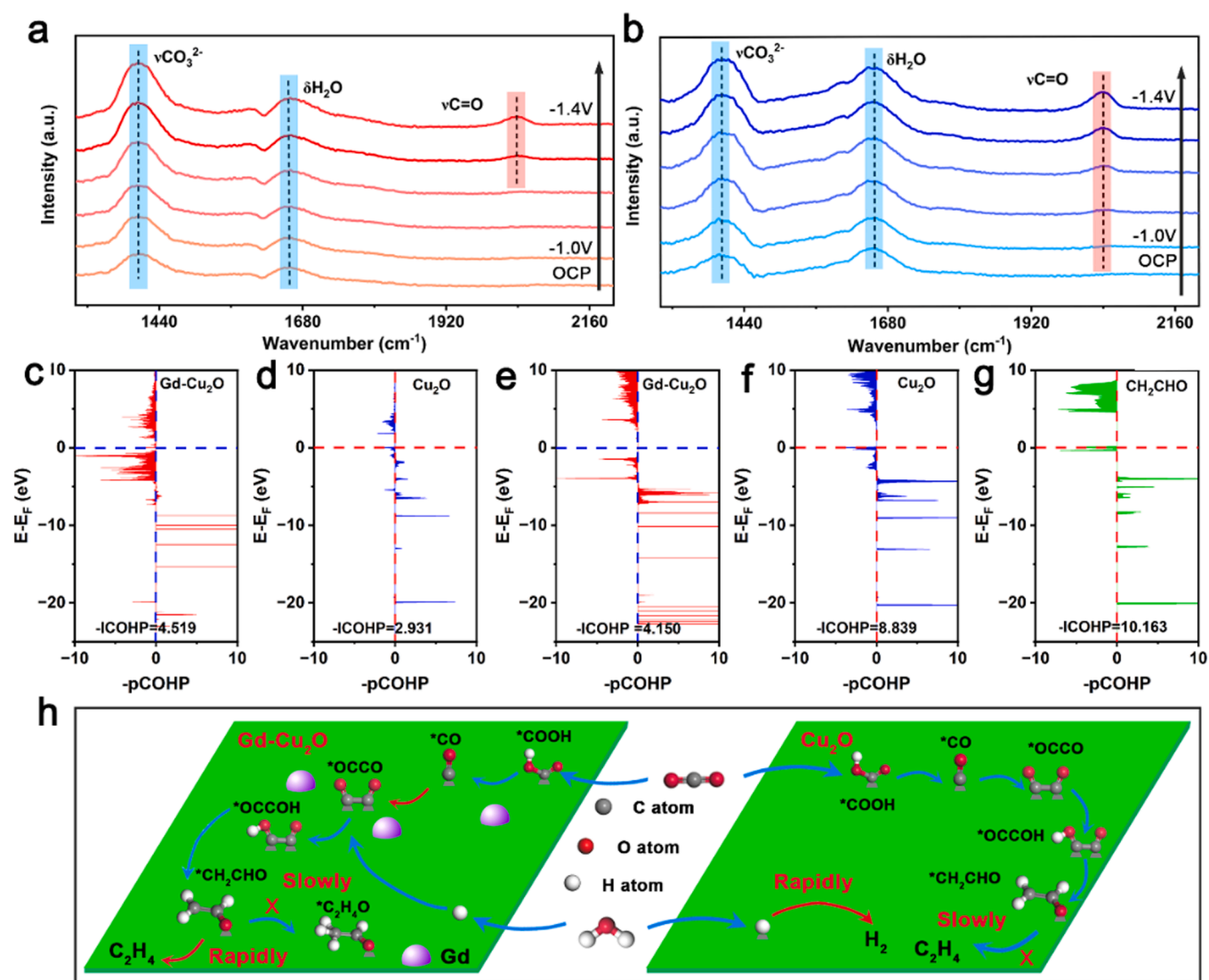


Fig. 5. In situ Fourier transform infrared (FTIR) of CO₂RR intermediates on (a) Cu₂O and (b) Gd-Cu₂O at different applied potentials in 0.5 M KHCO₃ electrolyte in a H cell reactor. Crystal orbital Hamilton populations (COHP) between *OCHCH₂ and Gd-Cu₂O (c) and Cu₂O (d). COHP of *OCHCH₂ absorbed on Gd-Cu₂O (e) *OCHCH₂ absorbed on Cu₂O (f), and pure *OCHCH₂ (g). (h) The supposed reaction mechanism of CO₂RR on the Gd-Cu₂O (left) and Cu₂O (right).

Gd-Cu₂O. Consequently, Gd-Cu₂O demonstrates enhanced *OCHCH₂ adsorption, attributed to stronger Cu-O bonds. This is further supported by pCOHP analysis of the C-O bonding orbitals in *OCHCH₂, as depicted in Fig. 5e-5g. The bonding orbitals of C-O in *OCHCH₂ adsorbed on Gd-Cu₂O (-ICOHP: 4.150) are less occupied than those on Cu₂O (-ICOHP: 8.839) and pure *OCHCH₂ (-ICOHP: 10.163), indicating a weaker C-O interaction on Gd-Cu₂O. This evidence robustly demonstrates that Gd introduction strengthens the Cu-O bond and weakens the C-O bond in *OCHCH₂, directing the reaction towards ethylene production. Bader charge analysis (Fig. S20) reveals more charge transfer from Cu to *OCHCH₂ on the Gd-Cu₂O surface compared to Cu₂O. Additionally, reduced charge transfer between *O-CHCH₂ implies a stronger Cu-O bond and a weaker *O-CHCH₂ bond, significantly improving ethylene selectivity. Fig. 5 h provides a schematic representation of the reaction pathway in CO₂ reduction. In the Gd-Cu₂O system, CO₂ molecules undergo rapid activation, leading to C-C coupling and the formation of the *OCHCH₂ intermediate. The incorporation of Gd alters the electron density at the Cu sites, resulting in electron enrichment. This enrichment strengthens the bond between Cu and *OCHCH₂ and concurrently facilitates the breaking of the *O-CHCH₂ bond, thereby enhancing the selectivity towards ethylene production. In contrast, CO₂ activation on Cu₂O surfaces poses significant challenges; the energy barrier for C-C coupling is elevated, and the cleavage of the *O-CHCH₂ bond in *OCHCH₂ is hindered, culminating in lower ethylene selectivity. Overall, the findings from DFT calculations indicate a preferential pathway for CO₂-to-C₂H₄ conversion on Gd-Cu₂O. This preference is attributed primarily to the effects of electron enrichment at the Cu sites and the associated reduction in C-O bond interaction strength.

4. Conclusion

In this study, we developed a Gd-Cu₂O catalyst that exhibits an electron enrichment effect at Cu sites, proving to be an effective electrocatalyst for the reduction of CO₂ to C₂H₄. The Gd-Cu₂O catalyst demonstrated stable production of C₂H₄ over a continuous 7-hour operation, outperforming the Cu₂O catalyst by achieving a C₂H₄ selectivity that was 1.42 times greater. Both experimental observations and DFT calculations corroborate that introducing Gd into Cu₂O enhances electron density at the Cu sites. Mechanistic analysis reveals that this electron enrichment at Cu sites in Gd-Cu₂O strengthens the interaction between Cu and the *OCHCH₂ intermediate, a stark contrast to what is observed in Cu₂O. Concurrently, it weakens the *O-CHCH₂ bond, leading to more efficient C-O bond cleavage and subsequently increased C₂H₄ selectivity. This work highlights the significant impact of modifying electron density in copper-based catalysts on intermediate adsorption, shedding light on their crucial role in dictating the activity and selectivity of the CO₂ reduction reaction.

CRedit authorship contribution statement

Xiaojun Wang: Investigation. **Zhiyu Yang:** Investigation, Conceptualization. **Huiying Zhang:** Writing – original draft, Investigation, Data curation, Conceptualization. **Zishan Hou:** Conceptualization. **Jinrui Wang:** Investigation. **Jiangzhou Xie:** Writing – original draft. **Kaiqi Nie:** Resources. **Zheng Tang:** Conceptualization. **Xiaoxuan Wang:** Investigation. **Xueying Gao:** Investigation. **Shuyuan Li:** Investigation. **Yanfei Sun:** Investigation. **Yi-Ming Yan:** Writing – original draft, Data curation, Conceptualization.

Declaration of Competing Interest

The authors declare that they have no known competing financial interests or personal relationships that could have appeared to influence the work reported in this paper.

Data Availability

Data will be made available on request.

Acknowledgements

Financial support from the National Natural Science Foundation of China (grant nos. 22379006, U20A20154, 22279005, 21575016) and from the National Program for Support of Top-notch Young Professionals is gratefully acknowledged. The numerical calculations in this paper have been done on Hefei advanced computing center.

Appendix A. Supporting information

Supplementary data associated with this article can be found in the online version at doi:10.1016/j.apcatb.2024.123992.

References

- [1] L. Yu, F. Li, J. Huang, B.G. Sumpter, W.E. Mustain, Z. Chen, Double-atom catalysts featuring inverse sandwich structure for CO₂ reduction reaction: a synergetic first-principles and machine learning investigation, *ACS Catal.* 13 (2023) 9616–9628.
- [2] S. Van Daele, L. Hintjens, S. Hoekx, B. Böhlen, S. Neukermans, N. Daems, J. Hereijgers, T. Breugelmans, How flue gas impurities affect the electrochemical reduction of CO₂ to CO and formate, *Appl. Catal. B Environ.* 341 (2024) 123345.
- [3] C. Yan, W. Luo, H. Yuan, G. Liu, R. Hao, N. Qin, Z. Wang, K. Liu, Z. Wang, D. Cui, Z. Hu, Y. Lan, Z. Lu, Stabilizing intermediates and optimizing reaction processes with N doping in Cu₂O for enhanced CO₂ electroreduction, *Appl. Catal. B Environ.* 308 (2022) 121191.
- [4] J. Kim, T.H. Ha, J. Kim, G.H. Jeong, S.O. Kim, W. Chung, K. Roh, J.H. Lee, J. Oh, Design principles for selective and economical CO₂ electrolysis in acids, *Appl. Catal. B Environ.* 339 (2023) 123160.
- [5] S.Z. Tianran Wei, Qian Liu, Yuan Qiu, Jun Luo, Xijun Liu, Oxygen vacancy-rich amorphous copper oxide enables highly selective electroreduction of carbon dioxide to ethylene, *Acta Phys. Chim. Sin.* 39 (2023) 2207026.
- [6] S. Gao, T. Wang, M. Jin, S. Zhang, Q. Liu, G. Hu, H. Yang, J. Luo, X. Liu, Bifunctional Nb-N-C atomic catalyst for aqueous Zn-air battery driving CO₂ electrolysis, *Sci. China Mater.* 66 (2023) 1013–1023.
- [7] L. Ji, L. Li, X. Ji, Y. Zhang, S. Mou, T. Wu, Q. Liu, B. Li, X. Zhu, Y. Luo, X. Shi, A. M. Asiri, X. Sun, Highly selective electrochemical reduction of CO₂ to alcohols on an FeP nanorarray, *Angew. Chem. Int. Ed.* 59 (2020) 758–762.
- [8] W. Liu, P. Zhai, A. Li, B. Wei, K. Si, Y. Wei, X. Wang, G. Zhu, Q. Chen, X. Gu, R. Zhang, W. Zhou, Y. Gong, Electrochemical CO₂ reduction to ethylene by ultrathin CuO nanoplate arrays, *Nat. Commun.* 13 (2022) 1877.
- [9] F.-Y. Gao, S.-J. Hu, X.-L. Zhang, Y.-R. Zheng, H.-J. Wang, Z.-Z. Niu, P.-P. Yang, R.-C. Bao, T. Ma, Z. Dang, Y. Guan, X.-S. Zheng, X. Zheng, J.-F. Zhu, M.-R. Gao, S.-H. Yu, High-curvature transition-metal chalcogenide nanostructures with a pronounced proximity effect enable fast and selective CO₂ electroreduction, *Angew. Chem. Int. Ed.* 59 (2020) 8706–8712.
- [10] J. Liu, P. Li, J. Bi, S. Jia, Y. Wang, X. Kang, X. Sun, Q. Zhu, B. Han, Switching between C₂⁺ products and CH₄ in CO₂ electrolysis by tuning the composition and structure of rare-Earth/Copper catalysts, *J. Am. Chem. Soc.* 145 (2023) 23037–23047.
- [11] M. Nur Hossain, S. Chen, A. Chen, Thermal-assisted synthesis of unique Cu nanodendrites for the efficient electrochemical reduction of CO₂, *Appl. Catal. B Environ.* 259 (2019) 118096.
- [12] Z. Gu, N. Yang, P. Han, M. Kuang, B. Mei, Z. Jiang, J. Zhong, L. Li, G. Zheng, Oxygen Vacancy Tuning toward Efficient Electrocatalytic CO₂ reduction to C₂H₄, *Small Methods* 3 (2019) 1800449.
- [13] S. Mou, Y. Li, L. Yue, J. Liang, Y. Luo, Q. Liu, T. Li, S. Lu, A.M. Asiri, X. Xiong, D. Ma, X. Sun, Cu₂Sb decorated Cu nanowire arrays for selective electrocatalytic CO₂ to CO conversion, *Nano Res.* 14 (2021) 2831–2836.
- [14] S. Mou, T. Wu, J. Xie, Y. Zhang, L. Ji, H. Huang, T. Wang, Y. Luo, X. Xiong, B. Tang, X. Sun, Boron Phosphide Nanoparticles: A Nonmetal Catalyst for High-selectivity Electrochemical Reduction of CO₂ to CH₃OH, *Adv. Mater.* 31 (2019) 1903499.
- [15] S. Gao, S. Chen, Q. Liu, S. Zhang, G. Qi, J. Luo, X. Liu, Bifunctional BiPd alloy particles anchored on carbon matrix for reversible Zn–CO₂ battery, *ACS Appl. Nano Mater.* 5 (2022) 12387–12394.
- [16] Y. Zhou, Y. Liang, J. Fu, K. Liu, Q. Chen, X. Wang, H. Li, L. Zhu, J. Hu, H. Pan, M. Miyauchi, L. Jiang, E. Cortés, M. Liu, Vertical Cu nanoneedle arrays enhance the local electric field promoting C₂ hydrocarbons in the CO₂ electroreduction, *Nano Lett.* 22 (2022) 1963–1970.
- [17] Y. He, F.H. Müller, R. Palkovits, F. Zeng, C. Mebrahtu, Tandem catalysis for CO₂ conversion to higher alcohols: a review, *Appl. Catal. B Environ.* 345 (2024) 123663.
- [18] H. Li, H. Zhou, Y. Zhou, J. Hu, M. Miyauchi, J. Fu, M. Liu, Electric-field promoted C–C coupling over Cu nanoneedles for CO₂ electroreduction to C₂ products, *Chinese J. Catal.* 43 (2022) 519–525.
- [19] B. Yang, K. Liu, H. Li, C. Liu, J. Fu, H. Li, J.E. Huang, P. Ou, T. Alkayyali, C. Cai, Y. Duan, H. Liu, P. An, N. Zhang, W. Li, X. Qiu, C. Jia, J. Hu, L. Chai, Z. Lin, Y. Gao,

- M. Miyauchi, E. Cortés, S.A. Maier, M. Liu, Accelerating CO₂ electroreduction to multicarbon products via synergistic electric–thermal field on copper nanoneedles, *J. Am. Chem. Soc.* 144 (2022) 3039–3049.
- [20] D.G. Park, J.W. Choi, H. Chun, H.S. Jang, H. Lee, W.H. Choi, B.C. Moon, K.-H. Kim, M.G. Kim, K.M. Choi, B. Han, J.K. Kang, Increasing CO binding energy and defects by preserving Cu oxidation state via O₂-plasma-assisted N doping on CuO enables high C₂₊ selectivity and long-term stability in electrochemical CO₂ reduction, *ACS Catal.* 13 (2023) 9222–9233.
- [21] G.-Y. Duan, X.-Q. Li, G.-R. Ding, L.-J. Han, B.-H. Xu, S.-J. Zhang, Highly efficient electrocatalytic CO₂ reduction to C₂₊ products on a poly(ionic liquid)-Based Cu⁰–Cu^I tandem catalyst, *Angew. Chem. Int. Ed.* 61 (2022) e202110657.
- [22] S. Kong, X. Lv, X. Wang, Z. Liu, Z. Li, B. Jia, D. Sun, C. Yang, L. Liu, A. Guan, J. Wang, G. Zheng, F. Huang, Delocalization state-induced selective bond breaking for efficient methanol electrosynthesis from CO₂, *Nat. Catal.* 6 (2023) 6–15.
- [23] D. Xiang, K. Li, M. Li, R. Long, Y. Xiong, D. Yakhvarov, X. Kang, Theory-guided synthesis of heterostructured Cu@Cu_{0.4}W_{0.6} catalyst towards superior electrochemical reduction of CO₂ to C₂ products, *Mater. Today Phys.* 33 (2023) 101045.
- [24] J. Bi, P. Li, J. Liu, S. Jia, Y. Wang, Q. Zhu, Z. Liu, B. Han, Construction of 3D copper-chitosan-gas diffusion layer electrode for highly efficient CO₂ electrolysis to C₂₊ alcohols, *Nat. Commun.* 14 (2023) 2823.
- [25] Y. Chen, W. Qu, T. Luo, H. Zhang, J. Fu, H. Li, C. Liu, D. Zhang, M. Liu, Promoting C-F bond activation via proton donor for CF₄ decomposition, *Proc. Natl. Acad. Sci.* 120 (2023) e2312480120.
- [26] Y.E. Kim, W. Lee, Y.N. Ko, J.E. Park, D. Tan, J. Hong, Y.E. Jeon, J. Oh, K.T. Park, Role of binder in Cu₂O Gas diffusion electrodes for CO₂ reduction to C₂₊ products, *ACS Sustain. Chem. Eng.* 10 (2022) 11710–11718.
- [27] A. Xu, S.-F. Hung, A. Cao, Z. Wang, N. Karmodak, J.E. Huang, Y. Yan, A. Sedighian Rasouli, A. Ozden, F.-Y. Wu, Z.-Y. Lin, H.-J. Tsai, T.-J. Lee, F. Li, M. Luo, Y. Wang, X. Wang, J. Abed, Z. Wang, D.-H. Nam, Y.C. Li, A.H. Ip, D. Sinton, C. Dong, E. H. Sargent, Copper/alkaline earth metal oxide interfaces for electrochemical CO₂-to-alcohol conversion by selective hydrogenation, *Nat. Catal.* 5 (2022) 1081–1088.
- [28] M. Zhang, Z. Zhang, Z. Zhao, H. Huang, D.H. Anjum, D. Wang, J.H. He, K. W. Huang, Tunable selectivity for electrochemical CO₂ reduction by bimetallic Cu–Sn catalysts: elucidating the roles of Cu and Sn, *ACS Catal.* 11 (2021) 11103–11108.
- [29] R. Chen, J. Zhao, Y. Li, Y. Cui, Y.-R. Lu, S.-F. Hung, S. Wang, W. Wang, G. Huo, Y. Zhao, W. Liu, J. Wang, H. Xiao, X. Li, Y. Huang, B. Liu, Operando Mössbauer spectroscopic tracking the metastable state of atomically dispersed Tin in copper oxide for Selective CO₂ electroreduction, *J. Am. Chem. Soc.* 145 (2023) 20683–20691.
- [30] H. Zhang, Y. Sun, J. Wang, X. Gao, Z. Tang, S. Li, Z. Hou, X. Wang, K. Nie, J. Xie, Z. Yang, Y.-M. Yan, Engineering CO bridge adsorption in Cu₂O-TiO₂ heterojunction catalyst for selective electrochemical CO₂ reduction to ethanol, *ACS Appl. Energy Mater.* 6 (2023) 11448–11457.
- [31] J. Feng, L. Wu, S. Liu, L. Xu, X. Song, L. Zhang, Q. Zhu, X. Kang, X. Sun, B. Han, Improving CO₂-to-C₂₊ product electroreduction efficiency via atomic lanthanide dopant-induced tensile-strained CuO_x catalysts, *J. Am. Chem. Soc.* 145 (2023) 9857–9866.
- [32] V. Okatenko, A. Loidice, M.A. Newton, D.C. Stoian, A. Blokhina, A.N. Chen, K. Rossi, R. Buonsanti, Alloying as a strategy to boost the stability of copper nanocatalysts during the electrochemical CO₂ reduction reaction, *J. Am. Chem. Soc.* 145 (2023) 5370–5383.
- [33] P. Wei, X. Li, Z. He, Z. Li, X. Zhang, X. Sun, Q. Li, H. Yang, J. Han, Y. Huang, Electron density modulation of MoP by rare earth metal as highly efficient electrocatalysts for pH-universal hydrogen evolution reaction, *Appl. Catal. B Environ.* 299 (2021) 120657.
- [34] H. Zhang, T. Luo, Y. Chen, K. Liu, H. Li, E. Pensa, J. Fu, Z. Lin, L. Chai, E. Cortés, L. Min, Highly efficient decomposition of perfluorocarbons for over 1000 Hours via active site regeneration, *Angew. Chem. Int. Ed.* 62 (2023) e202305651.
- [35] J. Li, W. Su, J. Li, L. Wang, J. Ren, S. Zhang, P. Cheng, H. Hong, D. Wang, Y. Zhou, W. Mi, Y. Du, Orientational alignment of oxygen vacancies: electric-field-inducing conductive channels in TiO₂ film to boost photocatalytic conversion of CO₂ into CO, *Nano Lett.* 21 (2021) 5060–5067.
- [36] Q. Fan, X. Zhang, X. Ge, L. Bai, D. He, Y. Qu, C. Kong, J. Bi, D. Ding, Y. Cao, X. Duan, J. Wang, J. Yang, Y. Wu, Manipulating Cu nanoparticle surface oxidation states tunes catalytic selectivity toward CH₄ or C₂₊ products in CO₂ electroreduction, *Adv. Energy Mater.* 11 (2021) 2101424.
- [37] Z.-Q. Liang, T.-T. Zhuang, A. Seifitokaldani, J. Li, C.-W. Huang, C.-S. Tan, Y. Li, P. De Luna, C.T. Dinh, Y. Hu, Q. Xiao, P.-L. Hsieh, Y. Wang, F. Li, R. Quintero-Bermudez, Y. Zhou, P. Chen, Y. Pang, S.-C. Lo, L.-J. Chen, H. Tan, Z. Xu, S. Zhao, D. Sinton, E.H. Sargent, Copper-on-nitride enhances the stable electrosynthesis of multi-carbon products from CO₂, *Nat. Commun.* 9 (2018) 3828.
- [38] Y. Zhao, X. Zu, R. Chen, X. Li, Y. Jiang, Z. Wang, S. Wang, Y. Wu, Y. Sun, Y. Xie, Industrial-current-density CO₂-to-C₂₊ electroreduction by anti-swelling anion-exchange ionomer-modified oxide-derived Cu nanosheets, *J. Am. Chem. Soc.* 144 (2022) 10446–10454.
- [39] W. Ma, S. Xie, T. Liu, Q. Fan, J. Ye, F. Sun, Z. Jiang, Q. Zhang, J. Cheng, Y. Wang, Electrocatalytic reduction of CO₂ to ethylene and ethanol through hydrogen-assisted C–C coupling over fluorine-modified copper, *Nat. Catal.* 3 (2020) 478–487.
- [40] Y. Yao, Y. Zhou, X. Liu, Y. Li, D. Wang, X. Chi, X. Wang, R. Zhao, H. Zhang, Y. Sun, Z.-Y. Yang, Y. Wei, Y.-M. Yan, Restraining lattice oxygen of Cu₂O by enhanced Cu–O hybridization for selective and stable production of ethylene with CO₂ electroreduction, *J. Mater. Chem. A* 10 (2022) 20914–20923.
- [41] Y. Yang, A. He, H. Li, Q. Zou, Z. Liu, C. Tao, J. Du, Operando constructing Cu/Cu₂O electrocatalysts for efficient CO₂ electroreduction to ethanol: CO₂-assisted structural evolution of octahedral Cu₂O by operando CV Activation, *ACS Catal.* 12 (2022) 12942–12953.
- [42] P. Li, J. Bi, J. Liu, Q. Zhu, C. Chen, X. Sun, J. Zhang, B. Han, In situ dual doping for constructing efficient CO₂-to-methanol electrocatalysts, *Nat. Commun.* 13 (2022) 1965.
- [43] Q. Wang, Y. Zhang, Y. Liu, K. Wang, W. Qiu, L. Chen, W. Li, J. Li, Photocorrosion behavior of Cu₂O nanowires during photoelectrochemical CO₂ reduction, *J. Electroanal. Chem.* 912 (2022) 116252.
- [44] P. Wang, H. Yang, Y. Xu, X. Huang, J. Wang, M. Zhong, T. Cheng, Q. Shao, Synergized Cu/Pb Core/shell electrocatalyst for high-efficiency CO₂ reduction to C₂₊ liquids, *ACS Nano* 15 (2021) 1039–1047.
- [45] W.P. Utomo, H. Wu, Y.H. Ng, Modulating the active sites of oxygen-deficient TiO₂ by copper loading for enhanced electrocatalytic nitrogen reduction to ammonia, *Small* 18 (2022) 2200996.
- [46] T. Shao, X. Wang, H. Dong, S. Liu, D. Duan, Y. Li, P. Song, H. Jiang, Z. Hou, C. Gao, Y. Xiong, Stacked plasmonic metamaterial with strong localized electric field enables highly efficient broadband light-driven CO₂ hydrogenation, *Adv. Mater.* 34 (2022) 2202367.
- [47] S.Y. Lee, H. Jung, N.-K. Kim, H.-S. Oh, B.K. Min, Y.J. Hwang, Mixed copper states in anodized Cu electrocatalyst for stable and selective ethylene production from CO₂ reduction, *J. Am. Chem. Soc.* 140 (2018) 8681–8689.
- [48] C.V. Prasad, M.S.P. Reddy, V. Rajagopal Reddy, C. Park, Effect of annealing on chemical, structural and electrical properties of Au/Gd₂O₃/n-GaN heterostructure with a high-k rare-earth oxide interlayer, *Appl. Surf. Sci.* 427 (2018) 670–677.
- [49] Z. Zhu, Q. Lv, Y. Ni, S. Gao, J. Geng, J. Liang, F. Li, Internal electric field and interfacial bonding engineered step-scheme junction for a visible-light-involved lithium–oxygen battery, *Angew. Chem. Int. Ed.* 61 (2022) e202116699.
- [50] X. Wang, X. Wan, X. Qin, C. Chen, X. Qian, Y. Guo, Q. Xu, W.-B. Cai, H. Yang, K. Jiang, Electronic structure modulation of RuO₂ by TiO₂ enriched with oxygen vacancies to boost acidic O₂ evolution, *ACS Catal.* 12 (2022) 9437–9445.
- [51] T.-T. Zhuang, Z.-Q. Liang, A. Seifitokaldani, Y. Li, P. De Luna, T. Burdyny, F. Che, F. Meng, Y. Min, R. Quintero-Bermudez, C.T. Dinh, Y. Pang, M. Zhong, B. Zhang, J. Li, P.-N. Chen, X.-L. Zheng, H. Liang, W.-N. Ge, B.-J. Ye, D. Sinton, S.-H. Yu, E. H. Sargent, Steering post-C–C coupling selectivity enables high efficiency electroreduction of carbon dioxide to multi-carbon alcohols, *Nat. Catal.* 1 (2018) 421–428.
- [52] Y. Zhang, J.-X. Liu, K. Qian, A. Jia, D. Li, L. Shi, J. Hu, J. Zhu, W. Huang, Structure sensitivity of Au–TiO₂ strong metal–support interactions, *Angew. Chem. Int. Ed.* 60 (2021) 12074–12081.
- [53] W. Ren, X. Tan, C. Jia, A. Krammer, Q. Sun, J. Qu, S.C. Smith, A. Schueler, X. Hu, C. Zhao, Electronic regulation of Nickel single atoms by confined Nickel nanoparticles for energy-efficient CO₂ electroreduction, *Angew. Chem. Int. Ed.* 61 (2022) e202203335.
- [54] X. Wang, X. Chi, Z. Fu, Y. Xiong, S. Li, Y. Yao, K. Zhang, Y. Li, S. Wang, R. Zhao, Z. Yang, Y.-M. Yan, Interfacial electric field triggered N₂ activation for efficient electrochemical synthesis of ammonia, *Appl. Catal. B Environ.* 322 (2023) 122130.
- [55] S. Shen, X. Peng, L. Song, Y. Qiu, C. Li, L. Zhuo, J. He, J. Ren, X. Liu, J. Luo, AuCu alloy nanoparticle embedded Cu submicrocone arrays for selective conversion of CO₂ to ethanol, *Small* 15 (2019) 1902229.
- [56] B. Deng, M. Huang, K. Li, X. Zhao, Q. Geng, S. Chen, H. Xie, Xa Dong, H. Wang, F. Dong, The crystal plane is not the key factor for CO₂-to-methane electrosynthesis on reconstructed Cu₂O microparticles, *Angew. Chem. Int. Ed.* 61 (2022) e202114080.
- [57] P.-P. Yang, X.-L. Zhang, F.-Y. Gao, Y.-R. Zheng, Z.-Z. Niu, X. Yu, R. Liu, Z.-Z. Wu, S. Qin, L.-P. Chi, Y. Duan, T. Ma, X.-S. Zheng, J.-F. Zhu, H.-J. Wang, M.-R. Gao, S.-H. Yu, Protecting copper oxidation state via intermediate confinement for selective CO₂ electroreduction to C₂₊ fuels, *J. Am. Chem. Soc.* 142 (2020) 6400–6408.
- [58] Y. Sun, J. Xie, Z. Fu, H. Zhang, Y. Yao, Y. Zhou, X. Wang, S. Wang, X. Gao, Z. Tang, S. Li, X. Wang, K. Nie, Z. Yang, Y.-M. Yan, Boosting CO₂ electroreduction to C₃H₄ via unconventional hybridization: high-order Ce⁴⁺ 4f and O 2p interaction in Ce–Cu₂O for stabilizing Cu⁺, *ACS Nano* 17 (2023) 13974–13984.
- [59] W. Ni, C. Li, X. Zang, M. Xu, S. Huo, M. Liu, Z. Yang, Y.-M. Yan, Efficient electrocatalytic reduction of CO₂ on Cu_xO decorated graphene oxides: an insight into the role of multivalent Cu in selectivity and durability, *Appl. Catal. B Environ.* 259 (2019) 118044.
- [60] Z.-Z. Wu, X.-L. Zhang, Z.-Z. Niu, F.-Y. Gao, P.-P. Yang, L.-P. Chi, L. Shi, W.-S. Wei, R. Liu, Z. Chen, S. Hu, X. Zheng, M.-R. Gao, Identification of Cu(100)/Cu(111) interfaces as superior active sites for CO dimerization during CO₂ electroreduction, *J. Am. Chem. Soc.* 144 (2022) 259–269.
- [61] Y. Qin, W. Zhang, F. Wang, J. Li, J. Ye, X. Sheng, C. Li, X. Liang, P. Liu, X. Wang, X. Zheng, Y. Ren, C. Xu, Z. Zhang, Extraordinary p–d hybridization interaction in heterostructural Pd–PdSe nanosheets boosts C–C Bond Cleavage of ethylene glycol electrooxidation, *Angew. Chem. Int. Ed.* 61 (2022) e202200899.
- [62] S. Chen, C. Ye, Z. Wang, P. Li, W. Jiang, Z. Zhuang, J. Zhu, X. Zheng, S. Zaman, H. Ou, L. Lv, L. Tan, Y. Su, J. Ouyang, D. Wang, Selective CO₂ reduction to ethylene mediated by adaptive small-molecule engineering of copper-based electrocatalysts, *Angew. Chem. Int. Ed.* 62 (2023) e202315621.
- [63] K. Das, R. Das, M. Riyaz, A. Parui, D. Bagchi, A.K. Singh, A.K. Singh, C.P. Vinod, S. C. Peter, Intrinsic charge polarization in Bi19S27Cl3 nanorods promotes selective C–C coupling reaction during photoreduction of CO₂ to ethanol, *Adv. Mater.* 35 (2023) 2205994.
- [64] S. Li, X. Wang, X. Chi, Y. Xiong, Y. Sun, Z. Tang, X. Gao, H. Zhang, J. Li, K. Nie, J. Xie, Z. Yang, Y.-M. Yan, Boosted N₂ activation through 4f–2p–3d orbital hybridization for efficient nitrate electrosynthesis, *Adv. Funct. Mater.* 33 (2023) 2306098.